In situ O$_2$-releasing quantum dot composites with enhanced radical scavenging behaviour, biosafety, and broadband UV shielding applications

Sayoni Sarkar [a], Atul Kumar Singh [b], Ajit R. Kulkarni [a,c*]

[a] Centre for Research in Nano Technology and Science, Indian Institute of Technology Bombay, Mumbai, India

[b] Central Research Facility (CRF), IIT Delhi Sonipat Campus, Haryana, India

[c] Department of Metallurgical Engineering and Materials Science, Indian Institute of Technology Bombay, Mumbai, India, E-mail: ajit.kulkarni@iitb.ac.in; Fax: +91-22-2572-3480; Tel: +91-22-25767636

Abstract: Understanding the defect-driven photophysics-surface chemistry interplay at the nanoscale further augments new design considerations for active ingredients for skin UV protection, emphasizing affordability, safety, and multi-functionality. Accelerating it, our study unravelled broad-spectrum UV attenuation (250 nm-400 nm) and long-lasting photostability (> 5 h) exhibited by in-house fabricated β-cyclodextrin functionalized, oxygen vacancy rich-CeO$_2$/ZnO quantum dots composites (V$_O{}^\bullet$-CeO$_{2(x)}$/ZnO$_{(1-x)}$@β-CD QD composites). A conceptually different strategy was pursued, involving artificially engineering surface V$_O{}^\bullet$ defects to modulate the band structure and enhance the molar absorptivity through photogenerated electron-hole separation. Unlike the conventional inorganic UV blockers, the QD composites harnessed their surface V$_O{}^\bullet$ to participate in a self-cascading antioxidant effect, scavenging 62.8% $^\bullet$OH radicals. Results indicated that autocatalytic endogenous O$_2$ generation from H$_2$O$_2$ scavenging accelerated by Ce^{3+}/Ce^{4+} couple begets anti-photoaging and sunburn alleviation. The bandgap-engineered QD composites demonstrated synergistic suppression of oxidative stress development and remarkable cell viability (≥90%) even under UV irradiation. These underlying principles can be extended to prevent and treat other ROS-induced skin ailments. Incorporating V$_O{}^\bullet$-CeO$_{2(0.3)}$/ZnO$_{(0.7)}$@β-CD QDs as active ingredients in commercial sunscreens unveiled a substantial enhancement in overall sun protection and antioxidative efficacy. Thus, it is envisioned that V$_O{}^\bullet$-CeO$_{2(x)}$/ZnO$_{(1-x)}$@β-CD QD composites hold promise for developing safe, efficacious, and economical sunscreens.

Keywords: Broad-band photoprotection, cascade antioxidant, anti-aging, surface oxygen vacancy, quantum dot composite

1. Introduction

It is well-known that prolonged exposure to ultraviolet radiation (UVR) imparts various deleterious effects on human skin, manifesting as sunburn, premature photoaging, and an increased risk of oxidative stress-induced cutaneous malignancies [1, 2]. Recent research

shows an alarming increase in incidences of UV-induced dermatological disorders attributed to ozone layer depletion [3]. The UVRs that ultimately reach the earth's surface are primarily composed of UVA (320-400 nm), with a small portion being UVB (290-320 nm), which leads to dermal phototoxicity [4]. The World Health Organization (WHO) reports that a staggering one in three individuals in the United States is now affected by detrimental UVRs [5]. Sunscreen use has been strongly recommended to combat the risk of UV-induced skin damage. Despite significant strides towards addressing concerns related to broad-spectrum UV screening and photosafety utilizing organic and nanostructured-inorganic UV shielding agents, several grey areas exist pertaining to their efficacy. Organic UV filters pose an elevated risk of skin inflammation and degradation. On the other hand, contemporary inorganic physical UV filters such as nano-ZnO and nano-TiO_2 have made a mark for their fascinating photophysics. As the dimensions of these inorganic physical blockers enlarge, sunscreen compositions manifest a whitish tinge upon application to the skin's surface. Such an effect is deemed unfavourable for the aesthetic appeal of the skin, thereby detracting from its desirability within the cosmetic industry. Moreover, nano-ZnO and nano-TiO_2 exhibit notable band-edge emission in the UVA regime ($\sim$ 370-380 nm), which contribute to the rapid photocatalytic degradation and oxidative stress development in the keratinocytes due to UV-induced-reactive oxygen species (ROS) generation. This oxidative imbalance leads to a range of dermatological concerns, including erythema, hyperpigmentation, and photo-aging among others [6,7]. Alternatives such as TiH_2, defect-rich ZnO quantum dots (QDs), CeO_2, and Fe_2O_3 nanoparticles have shown potential as UV shielding agents [8-12]. Regardless, their photostability, skin-friendly properties, toxicity in high doses, and sunscreen efficacy with respect to their commercial counterparts are rarely explored. Consequently, the quest for an ideal multifunctional UVR absorbent that fulfills the "all-in-one" functionalities — broad-spectrum photoprotection, benign, antioxidant, and good sensory features, aligning with evolving paradigms and mechanisms, is indispensable, albeit challenging. Trade-offs exist between these design considerations, cost, aesthetic appeal, and nuanced photoprotection mechanisms.

Globally recognized for their sun protection benefits in skin care products, nano-metal oxide UV filters carry potential toxicity risks due to their inherent photocatalytic properties. Introducing controlled defects in metal oxides can reduce photocatalytic response through systematic electron-hole separation and enhance safety. Conventional defect engineering methods involving dopant-mediated fabrication are costly and hazardous. Previously, we

introduced a dopant-free seed mediated continuous flow synthesis concept to engineer singly ionized oxygen vacancy ($V_O^\bullet$) defects in ZnO QDs, amplifying photoprotection efficacy by eliminating the detrimental characteristic UVA emission. These $V_O^\bullet$-rich ZnO QDs serve as non-toxic, antioxidant, and bioactive ingredients in sunscreens with high molar absorptivity [9]. This delineated the importance of defect chemistry in modulating the photophysics and photobiology of semiconductor nanomaterials. Nevertheless, their effectiveness is limited to lower doses, potentially inadequate for extended usage in skincare and cosmetics. Thus, we hypothesized that preferentially modifying $V_O^\bullet$-rich ZnO QDs by incorporating varying proportions of $V_O^\bullet$-rich CeO_2 QDs would result in a QD composite with unprecedented UV shielding effects and bioactivity. While acknowledged for their photo-redox capabilities, CeO_2 QDs are hindered by their limited transparency when applied on the skin, curbing their extensive use in sunscreens. By designing $V_O^\bullet$-$CeO_{2(x)}/ZnO_{(1-x)}@\beta$-CD QD composite system to mimic the natural fluorescence of human skin via $V_O^\bullet$-mediated photophysics, the goal is to overcome this limitation and expand the potential commercial applications in dermatological UV protection and biomedicine. Nonetheless, bare metal oxide QDs have confined use in biomedicine because of their agglomeration tendency in the physiological milieu, compromising biocompatibility. To ameliorate this, we employed an "eco-friendly" biodegradable and cost-effective oligosaccharide — β-cyclodextrin (β-CD) to modify the surface of $V_O^\bullet$-$CeO_{2(x)}/ZnO_{(1-x)}$ QD composites and stabilize them through "host-guest" inclusion complexes ($V_O^\bullet$-$CeO_{2(x)}/ZnO_{(1-x)}@\beta$-CD QD composites) [13].

Herein, we present $V_O^\bullet$-$CeO_{2(x)}/ZnO_{(1-x)}@\beta$-CD QD composites for the first time as a low-cost multifunctional physical active ingredient. Our study delves into the influence of surface $V_O^\bullet$, artificially engineered by incorporating $V_O^\bullet$-rich CeO_2 QDs in $V_O^\bullet$-rich ZnO QDs on broad-spectrum photoprotection, prolonged photostability, enhanced transparency for aesthetic appeal, cascade antioxidant effects, alleviation of UV-induced toxicity, and augmentation of skin sensorial features. Mechanistic insights into these effects are derived from understanding their structural intricacies, photonics, and bio-activity. Additionally, the enhancement of UV attenuation, antioxidant performance, and biocompatibility of commercial sunscreens upon integrating $V_O^\bullet$-$CeO_{2(0.3)}/ZnO_{(0.7)}@\beta$-CD QDs is rationalized through a distinct set of experiments. Hence, in this study, the goal of developing a "superpower" UV blocker has been realized by the design and fabrication of novel $V_O^\bullet$-$CeO_{2(x)}/ZnO_{(1-x)}@\beta$-CD QD composites, paving the way for new-generation sunscreens.

2. Experimental details

2.1 Materials

Zinc acetate dihydrate (99.99 %), Cerium nitrate hexahydrate (99.99%), ammonia solution (30%), lithium hydroxide ($\geq$ 98%, analytical grade), titanium dioxide nanoparticles (TiO_2 NPs), 3-(4, 5-dimethylthiazol-2-yl)-2, 5-diphenyltetrazolium bromide (MTT) assay, N,N-Dimethylformamide (DMF), 2′, 7′-dichlorofluorescin diacetate (DCFDA), were supplied by Sigma Aldrich, US. β-CD (> 99%) was procured from TCI chemicals, India. Terephthalic acid and rhodamine 6G were obtained from Loba Chemie, India. All the chemicals were of analytical grade and used as received. Hydrogen peroxide (H_2O_2) (30%) was purchased from Merck, Germany. Trypan blue assay, Dulbecco's phosphate buffered solution (DPBS), Dulbecco's modified Eagle's medium (DMEM), foetal bovine serum (FBS), antibiotics, and trypsin were purchased from HiMedia Laboratories (India). All studies used Milli-Q water.

2.2 Preparation of β-CD modified $V_O^\bullet$ rich-CeO_2/ZnO quantum dots ($V_O^\bullet$-$CeO_{2(x)}$/$ZnO_{(1-x)}$@β-CD QDs) composites

A two-step kinetically-controlled continuous flow synthesis is performed in an oxygen-deficient milieu to fabricate $V_O^\bullet$-$CeO_{2(x)}$/$ZnO_{(1-x)}$@β-CD QD composites. In the first step, $V_O^\bullet$ rich-ZnO QDs (0.1 M) and $V_O^\bullet$ rich-CeO_2 QDs (0.1 M) are separately synthesized, following one of our previously outlined procedure.[9] The engineering of abundant $V_O^\bullet$ by the accelerated nucleation-growth kinetics is facilitated by superior heat transfer characteristics in the reactor under oxygen deficient environment and precisely monitored hydrodynamics.

In the second step, varying concentrations of the as-prepared CeO_2 and ZnO QDs, as specified in Table 1, are directed to the reaction zone by the peristaltic pumps. After completion of the reaction, $V_O^\bullet$-$CeO_{2(x)}$/$ZnO_{(1-x)}$ QDs, collected in an ice bath at the output end, are transferred to a biphasic gas–liquid three-neck flask. To this, the β-CD solution, prepared in an 80% water-20% DMF mixture, is added under an N_2 gas flow to maintain minimal oxygen. Additionally, a 30% ammonia solution is added under an inert environment to ensure a pH of 10 for effective surface functionalization of the QDs with β-CD. The colloidal solution of $V_O^\bullet$-$CeO_{2(x)}$/$ZnO_{(1-x)}$@β-CD QD composites is vigorously stirred at 2500 rpm until slight turbidity is observed. Finally, following centrifugation and rigorous washing, the precipitate is dried overnight in a vacuum oven at 50°C. The resultant powdered $V_O^\bullet$-$CeO_{2(x)}$/$ZnO_{(1-x)}$@β-CD QD composites are dispersed in Milli-Q for further materials characterization and biological studies.

2.3 Characterization

X-ray diffraction studies are performed in a PANalytical Empyrean powder diffractometer. The spectra are acquired for the 2θ range of 20° to 80° employing Cu Kα radiation (λ) of 1.5406 Å to analyze the crystal structure, phase purity, and crystallite size. A Tecnai G2, F30 transmission electron microscope (TEM) (acceleration voltage of 300 kV) is employed to determine the size distribution and morphology. The samples are characterized further using high-angle annular dark field scanning transmission electron microscopy (HAADF-STEM) and energy dispersive spectroscopy (EDS) to evaluate their chemical composition. A Kratos Analytical, AXIS Supra is employed to perform X-ray photoelectron spectroscopy (XPS) to analyse the surface chemical composition and changes in the chemical environment by estimating Ce^{3+}/Ce^{4+} ratio, fraction of surface oxygen vacancies ($V_O^\bullet$), and tracking the shifts in the binding energies. CASAXPS software is used for peak fitting functions and background subtraction. The operational parameters included a monochromatic Al Kα source (1486.6 eV). Electron paramagnetic resonance (EPR) spectra are acquired at room temperature on a JES-FA200 spectrometer with 9.446 GHz microwave frequency and in X-band mode. FTIR spectra are obtained using a JASCO FT/IR-600 spectrometer to comprehensively analyze the IR-active functional groups denoting the surface chemistry.

Band gaps of the samples are calculated from the absorbance spectra measured with a JASCO V-570 in the 350-550 nm spectrum. Photoluminescence (PL) spectroscopy is performed using a HORIBA Fluoromax-4 Spectrofluorometer and HORIBA Jobin Yvon Fluorolog 3 spectrofluorometer to understand the role of $V_O^\bullet$ in regulating the emissive characteristics of the samples. These experiments facilitate the identification of the peak in the UVA (λ_{UV}) and the peak associated with the defect ($V_O^\bullet$)-mediated emission (λ_{VIS}). The colloidal stability of the samples, suspended in simulated body fluid (SBF) and DMEM (cell culture media), designed to mimic the biological microenvironment, is systematically assessed over a predetermined time interval. This evaluation was conducted utilizing a ZetaSizer Nano-ZS (Malvern Instruments).

2.4 Quantification of photo-induced ROS generation *in vitro*, and $^\bullet$OH detection

The assessment of photo-triggered endogenous ROS production is carried out using the DCFDA assay. In the presence of ROS, DCFDA undergoes oxidation to form DCF, characterized by its distinct fluorescence. The variations in fluorescence intensity are proportional to the fraction of ROS generated in the intracellular milieu. HaCaT cells are exposed to 50, 100, and 200 μg/mL of $V_O^\bullet$-$CeO_{2(0.3)}/ZnO_{(0.7)}@\beta$-CD QD composite, along with

nano-TiO$_2$, followed by UV irradiation (3 mW/cm^2 for 4 h). Further details of UVR exposure measurement are provided in section 2.3.1 of the supplementary information. The control experiment consists of cells incubated in the dark without treatment. Ensuing 24 h of incubation, 10 µm DCFDA is added and kept in the incubator for 30 mins (37°C, and 5% CO$_2$). Next, the DCF fluorescence is measured (excitation wavelength = 485 nm, emission wavelength = 520 nm) by the microplate reader and quantified to elucidate the ROS levels in the cells.

The hydroxyl radical ($^\bullet$OH) is a lethal ROS that serves as the primary mediator accountable for a substantial portion of DNA damage induced by UVRs. Thus, $^\bullet$OH producing or scavenging behaviour of the QDs is probed via the terephthalic acid (TPA) assay, employing PL spectroscopy to monitor fluorescent changes. Briefly, 10 µM H$_2$O$_2$ is added to 100 µg/mL of V$_O^\bullet$-CeO$_{2(0.3)}$/ZnO$_{(0.7)}$@β-CD QD composite, followed by UV irradiation. Subsequently, these samples are mixed with TPA solution in PBS and maintained at room temperature inside an orbital shaker incubator in the dark for 30 mins. Finally, fluorescence is detected at 430 nm using a HORIBA Fluoromax-4 Spectrofluorometer. Under UVR and in the presence of H$_2$O$_2$, TPA reacts with $^\bullet$OH to produce the fluorescent 2-hydroxy terephthalic acid (TAOH). A decrease in the PL intensity evident in the measurements can be attributed to the scavenging efficacy of the QDs.

2.5 Evaluation of cytotoxic effects

The biocompatibility of V$_O^\bullet$-CeO$_{2(0.3)}$/ZnO$_{(0.7)}$@β-CD QD composite at different dosages are studied in two cell lines – mouse fibroblast (L929) and human keratinocyte (HaCaT) cells. The cells are seeded in two separate 96-well plates at a density of 7.8×10^4 cells per well and placed in the incubator for 24 h to allow them to adhere. Next, the wells are washed thoroughly with PBS, and fresh DMEM is added to them. At 80% confluency, the cells are treated with 50, 100, and 200 µg/mL of the samples and incubated for 24 h. The wells are washed with PBS post-incubation, after which, MTT (100 µL/well) is added. Following the incubation for 3 h, DMSO (100 µL) is added to dissolve the formazan crystals. The cell survival rate is determined by collecting the absorbance spectra at 570 nm using a Tecan Infinite M200 PRO microplate reader.

Additional experiments involving HaCaT and L929 cells are undertaken to discern the critical impact of UV filters in protecting the skin from detrimental UVR-induced damage. The experimental framework is like the one outlined previously, except that the samples are

irradiated with UVR (3 mW/cm^2 for 4 h), prior to their addition, followed by a co-incubation period of 24 h. Cells without any treatment serve as the control group. The MTT assay is executed using a methodology analogous to that described for conditions without UV irradiation. The percentage of viable cells is calculated from the absorbance data acquired using the microplate reader (Tecan Infinite M200 PRO) at 570 nm.

2.6 Comparison of the photo-protection performance, antioxidant efficacy, and biosafety of $V_O{}^\bullet$-CeO$_{2(0.3)}$/ZnO$_{(0.7)}$@β-CD QD composite with nano-TiO$_2$-based (CS1) and nano-Al$_2$O$_3$ based (CS2) commercial sunscreen formulations

Separate sunscreen formulations integrating CS1 (SPF 30) and CS2 (SPF 50) with $V_O{}^\bullet$-CeO$_{2(0.3)}$/ZnO$_{(0.7)}$@β-CD QDs composite, respectively, are prepared by ultrasonic mixing for 15 mins to achieve homogeneity in the nanosuspension. The concentration of QDs in CS1 and CS2 varies based on the experimental objectives. $V_O{}^\bullet$-CeO$_{2(0.3)}$/ZnO$_{(0.7)}$@β-CD QD composite is selected among the other QDs due to their optimal photoprotective efficiency, photostability, camouflaging ability, biocompatibility, and ROS scavenging potency. Furthermore, the strategic choice of employing two sunscreens with distinct SPF values is driven by the rationale to evaluate the potential of $V_O{}^\bullet$-CeO$_{2(0.3)}$/ZnO$_{(0.7)}$@β-CD QD composite in enhancing the performance of high-SPF sunscreens.

Steady-state photoluminescence (PL) spectroscopy is employed to delineate the UV attenuation and emission characteristics of the modified sunscreen formulations. Increasing concentrations of $V_O{}^\bullet$-CeO$_{2(0.3)}$/ZnO$_{(0.7)}$@β-CD QD composite (50, 75, 100, 125 μg/mL) are mixed with CS1 and CS2, and PL spectra of the corresponding nanosuspensions are measured with a HORIBA Fluoromax-4 Spectrofluorometer. The spectral shifts and changes in the PL intensity are monitored to assess and compare the photoactivity of $V_O{}^\bullet$-CeO$_{2(0.3)}$/ZnO$_{(0.7)}$@β-CD QD composite with individual CS1 and CS2 formulations.

The alterations in photodegradation activity of the following catalysts: CS1, CS2, CS1+ $V_O{}^\bullet$-CeO$_{2(0.3)}$/ZnO$_{(0.7)}$@β-CD QD composite, CS2+ $V_O{}^\bullet$-CeO$_{2(0.3)}$/ZnO$_{(0.7)}$@β-CD QD composite, and $V_O{}^\bullet$-CeO$_{2(0.3)}$/ZnO$_{(0.7)}$@β-CD QD composite, are studied by analysing the rhodamine 6G (Rh6G) degradation under UV irradiation. The experimental procedure involves ultrasonic mixing of 50 μg/mL catalyst in Rh6G solution. Subsequently, they are subjected to UV radiation (365 nm) for 180 mins. The apparent changes in the photoluminescence of the samples are captured with a digital camera, both in visible light and UV irradiation conditions.

For the same set of samples, UVR-stimulated antioxidant efficacy of the modified and original sunscreen formulations is examined and compared by employing the terephthalic acid assay for $^{\bullet}$OH scavenging activity and the DCFDA assay for detecting the intracellular ROS generation in HaCaT cells. The experimental protocol is similar to that explained in section 2.4, wherein the cells are subjected to a treatment with 50, 100, and 200 μg/mL of the sample suspensions, along with UVR exposure. While the control group is comprised of untreated cells maintained in the dark. The oxidation of DCFDA to DCF, resulting from reactions with free radicals, is indicated by changes in the fluorescence profile of DCF as measured by the microplate reader (excitation wavelength = 485 nm, emission wavelength = 520 nm). The experiments are repeated thrice to ensure reproducibility.

The UVR-induced toxicity of the sunscreen formulations is ascertained using the MTT assay on HaCaT and L929 cells. An analogous procedure, as mentioned in section 2.5, is performed. The treatment consists of 50, 100, and 200 μg/mL of sample suspensions, ensuing a prolonged UVR exposure (3 mW/cm^2 for 4 h). This investigation emphasizes the significant modifications in the photosafety behaviour of the original sunscreen formulations upon the addition of $V_O^{\bullet}$-$CeO_{2(0.3)}$/$ZnO_{(0.7)}$@β-CD QD composite.

2.7 Statistical analysis

Experiments were replicated thrice, and data were presented as mean ± standard deviation. Statistical analyses utilized one-way ANOVA with Tukey's post-hoc test. For *p < 0.05*, data were considered to be statistically significant.
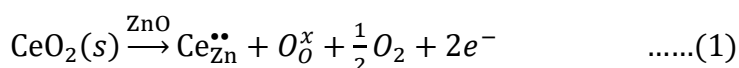
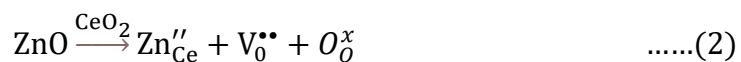## 3. Results and discussion

3.1 Phase analysis

The structural intricacies involving crystalline nature and phase purity of the $V_O^{\bullet}$-$CeO_{2(x)}$/$ZnO_{(1-x)}$@β-CD QD composites (x=0.1-0.9; Δx=0.1) are analyzed by XRD patterns as shown in Fig 1e. The apparent broadening of peaks affirms the ultrasmall size of the composites and lattice strain due to abundant oxygen vacancy defects. Pristine $V_O^{\bullet}$ rich-ZnO QDs exhibit diffraction peaks indexed to (100), (002), (101), (102), (110), (103), and (112) planes that correlate well with the hexagonal wurtzite crystal structure, according to JCPDS-ICDD index card no. 36–1451 [9]. Nevertheless, as the concentration of $V_O^{\bullet}$ enriched-CeO_2 QDs in ZnO progressively increases to 20%, a distinct peak emerges at the (111) plane, corresponding to CeO_2 with a fluorite crystal structure (JPCDS 34-0394) [14]. These observations emphasize

that the $V_O^\bullet$-$CeO_{2(x)}$/$ZnO_{(1-x)}$@β-CD QDs form a solid solution when $f_{[CeO_2]/([CeO_2]+[ZnO])} = 0.9$ or $f_{[CeO_2]/([CeO_2]+[ZnO])} = 0.1$. Increasing CeO_2 concentration beyond 60% causes noticeable peak shifts to lower 2θ values relative to pristine $V_O^\bullet$ rich-ZnO QDs. This peculiarity in the diffraction pattern of the QD composites can be explained by the substitution of Zn^{2+} by Ce^{4+}, possessing a larger ionic radius (0.97 Å) than Zn^{2+} (0.74 Å), which leads to the expansion of the crystal lattice.[15, 16] Consequently, crystallite size calculated from Debye Scherrer's relation (Fig 1d) decreases proportionally with a higher fraction of Ce^{4+} being incorporated in the Zn^{2+} site, suggesting the high potency of the continuous flow synthesis approach. It is important to note that had Zn^{2+} replaced Ce^{4+}, the lattice would have undergone contraction due to the former's smaller ionic radii, leading to shifting of 2θ to higher angles. However, such shifts are not perceived in the XRD pattern of $V_O^\bullet$-$CeO_{2(x)}$/$ZnO_{(1-x)}$@β-CD QD composites. Hence, the possibility of Zn^{2+} substituting Ce^{4+} can be undeniably ruled out.

3.2 Morphology, size, and composition

The TEM micrographs of $f_{[CeO_2]/([CeO_2]+[ZnO])} = 0.9$, 0.3, and 0.1 confirmed the quasi-ovular morphology and monodispersity among the QDs (Fig 1a, b, c). Intriguingly, no significant variations in morphology and homogeneity are observed with increasing CeO_2 content due to appropriate surface modification with β-CD and precisely controlled nucleation-growth kinetics [17]. The average particle dimensions, determined from HR-TEM images, were 2.79 nm for $f_{[CeO_2]/([CeO_2]+[ZnO])} = 0.9$ (smallest), 7.40 nm for $f_{[CeO_2]/([CeO_2]+[ZnO])} = 0.3$, and 9.16 nm for $f_{[CeO_2]/([CeO_2]+[ZnO])} = 0.1$. The increasing CeO_2 concentration in ZnO QDs can rationalize this dramatic size reduction, corroborating the Zener pinning mechanism that inhibits grain growth [18, 19]. Moreover, HR-TEM images of $f_{[CeO_2]/([CeO_2]+[ZnO])} = 0.3$ reveal the presence of lattice fringes with an inter-planar spacing of 0.31 and 0.26 nm, accredited to the (111) plane and (101) plane of CeO_2 and ZnO, respectively. A clear interface between CeO_2 and ZnO is discernible in $f_{[CeO_2]/([CeO_2]+[ZnO])} = 0.3$, which conforms well with the XRD data, implying partial substitution of Ce^{4+} in the Zn^{2+} site. While no phase separation occurs for $f_{[CeO_2]/([CeO_2]+[ZnO])} = 0.1$ and $f_{[CeO_2]/([CeO_2]+[ZnO])} = 0.9$, specifying the solubility limit. As a matter of fact, the radii of Ce^{3+} (1.14 Å) being much larger than Zn^{2+}, substituting the former in the latter's site is deemed implausible per Hume-Rothery's rule [20]. Here, only two probabilities are feasible, namely:

$$CeO_2(s) \xrightarrow{ZnO} Ce_{Zn}^{\bullet\bullet} + O_O^x + \frac{1}{2}O_2 + 2e^- \qquad ......(1)$$

$$ZnO \xrightarrow{CeO_2} Zn''_{Ce} + V_0^{\bullet\bullet} + O_O^x \qquad\qquad ......(2)$$

However, case (2) can be ruled out based on the XRD analysis. EDS line scan, acquired along the straight line demarcated in the HAADF-STEM images (Fig S1) of $f_{[CeO_2]/([CeO_2] + [ZnO])} = 0.3$, substantiate the atomic percentages of Ce, Zn, and O that are commensurate with what is anticipated from the synthesis. The corresponding EDS elemental maps indicate a uniform distribution of Ce, Zn, and O in the QDs.

Figure 1. HR-TEM image and size distribution plot of (a) $f_{[CeO_2]/([CeO_2] + [ZnO])} = 0.9$, (b) $f_{[CeO_2]/([CeO_2] + [ZnO])} = 0.3$, and (c) $f_{[CeO_2]/([CeO_2] + [ZnO])} = 0.1$, respectively. The upper right inset in the HR-TEM images show the presence of lattice fringes. The $V_O{}^\bullet$-$CeO_{2(x)}/ZnO_{(1-x)}$@β-CD QD composites are demarcated by dotted ovals. (d) Plot denoting relationship of crystallite size with varying $f_{[CeO_2]/([CeO_2] + [ZnO])}$ (e) XRD patterns.

3.3 Evaluating the role of artificially engineered surface $V_O{}^\bullet$ defects in augmenting photoprotection

XPS plots of $V_O^\bullet$-$CeO_{2(x)}/ZnO_{(1-x)}$@β-CD QDs (Fig 2) highlight the local chemical structure perturbations stemming from artificially engineering of surface $V_O^\bullet$. This is evidenced by anomalous shifts in Zn $2p_{3/2}$ and Zn $2p_{1/2}$ peaks to lower binding energies at 1018.01 eV and 1041.17 eV, respectively [21]. The surface $[Ce^{3+}]/([Ce^{3+}] + [Ce^{4+}])$ determined from the cumulative peak areas decreased from 59% in pristine $V_O^\bullet$ rich-CeO_2 QDs to 37.7% in $f_{[CeO_2]/([CeO_2] + [ZnO])} = 0.1$, cohering well with reducing CeO_2 content in the QD composite, as shown in Table 1. The initial drop in surface Ce^{3+} concentration is drastic with diminishing CeO_2 fractions until $f_{[CeO_2]/([CeO_2] + [ZnO])} = 0.6$, after which it nearly plateaus off. Notionally, the remarkably high Ce^{3+} and $V_O^\bullet$ in $V_O^\bullet$-$CeO_{2(x)}/ZnO_{(1-x)}$@β-CD QD composites is speculated to result from the replacement of Zn^{2+} by Ce^{4+} and the ultrasmall particle size (quantum size effect). Possibly the synthesis of the QDs in a kinetically regulated, oxygen-restricted environment further ameliorates the Ce^{3+} and $V_O^\bullet$ concentration, accelerating surface reactivity. From surface $V_O^\bullet$ percentages for all compositions enlisted in Table 1, it is ascertained that formation of the QD composites by introducing an optimum percentage of $V_O^\bullet$ rich-CeO_2 QDs in $V_O^\bullet$ rich-ZnO QDs is favourable for maximizing surface $V_O^\bullet$. These results agree with the EPR spectra (Fig 3b), unveiling a discrete signal at g = 2.004 ascribed to surface $V_O^\bullet$ (singly ionized oxygen vacancies) [22]. The signal intensity corresponding to g = 2.004 decreases steadily as a function of $V_O^\bullet$ concentration. In comparison to $V_O^\bullet$-$CeO_{2(x)}/ZnO_{(1-x)}$@β-CD QD composites, the signal at g = 1.96, attributable to Zn^+ or V_{Zn}^- or Ce^{3+}, is more pronounced in pristine $V_O^\bullet$ rich-ZnO QDs and $V_O^\bullet$ rich-CeO_2 QDs [23, 24]. These have implications for the effective separation of photogenerated carriers, altering photophysics and widening the UV attenuation spectrum.

Table 1. Comparison of crystallite size, particle size, and surface Ce^{3+} and $V_O^\bullet$ concentration of $V_O^\bullet$-$CeO_{2(x)}/ZnO_{(1-x)}$@β-CD QD composites (x=0.1-0.9; Δx=0.1)

[CeO₂]/[ZnO] ratio	Composition (in %)		Crystallite size[a] (in nm)	Particle size[b] (in nm)	%[Ce³⁺]/([Ce³⁺] + [Ce⁴⁺])[c]	% Vo/ (Vo + O_{L-Zn} + O_{L-Ce})[d]
	CeO₂	ZnO				
1.0	100	0	2.7	3.5	59.0	72.6
0.9	90	10	2.0	2.8	54.9	68.6
0.8	80	20	2.6	3	50.3	61.2
0.7	70	30	3.5	3.7	48.1	58.1
0.6	60	40	4.1	4.4	47.6	54.4
0.5	50	50	4.8	5.1	46.9	51.2
0.4	40	60	5.4	6.4	45.7	50.7

0.3	30	70	7.2	7.5	44.6	49.9
0.2	20	80	7.9	8.6	43.8	49.1
0.1	10	90	8.5	9.0	42.1	48.5
0.0	0	100	8.7	9.3	0.0	42.8

[a]Estimated from XRD data (Figure 1e), [b]Measured from TEM images, [c]Determined from Ce 3d XPS spectra (Fig 2d-h), [d]Calculated from O 1s XPS spectra (Figure 2c.)

The diverse optical absorption and emissive properties of QD composites with varying surface $V_O^\bullet$ concentrations in the UV-visible regime are investigated. The UV absorption characteristics of aqueous nanoformulations of $f_{[CeO_2]/([CeO_2] + [ZnO])}$ = 0.9, 0.3, and 0.1 are studied, as depicted in Fig 3c. The spectral changes demonstrate a pronounced red-shift in absorption band-edge compared to pristine $V_O^\bullet$ rich-ZnO QDs, with increasing CeO_2 concentration. This is a consequence of artificially incorporating surface $V_O^\bullet$ defects that give rise to mid-gap states. Our previous research showed promising band gap tunability in ZnO QDs through solely engineering native $V_O^\bullet$ defects, without resorting to any form of doping [9]. In a similar vein, Chen et al., articulated a simple concept of introduction of defects in the surface layers of nano-TiO_2 to modulate the band energies and allow carrier trapping to overcome the limited optical absorption [25]. Based on the premise of disorder induced-band structure modification, the pristine $V_O^\bullet$ rich-ZnO QDs and $V_O^\bullet$ rich-CeO_2 QDs display fair absorption potential in the UV spectrum but not in the visible light spectrum [26, 27]. Alternatively, the QD composites manifest superior broad-spectrum absorption in the entire UV-visible regime, starkly contrasting to most commercially available nano-TiO_2 or ZnO-based sunscreens and those containing organic UV filters. The entrapment of free electrons generated during UV irradiation by intermediate $V_O^\bullet$ levels could impede electron-hole recombination, thereby contributing to the nuanced photo-response. This phenomenon is reflected in the red-shifted UV absorption spectra of the QD composites, which exhibit band tail states often extending below the minima of the conduction band. Therefore, these defect centres serve as predominant determinants for the intraband transitions, consequently altering the optical profile.
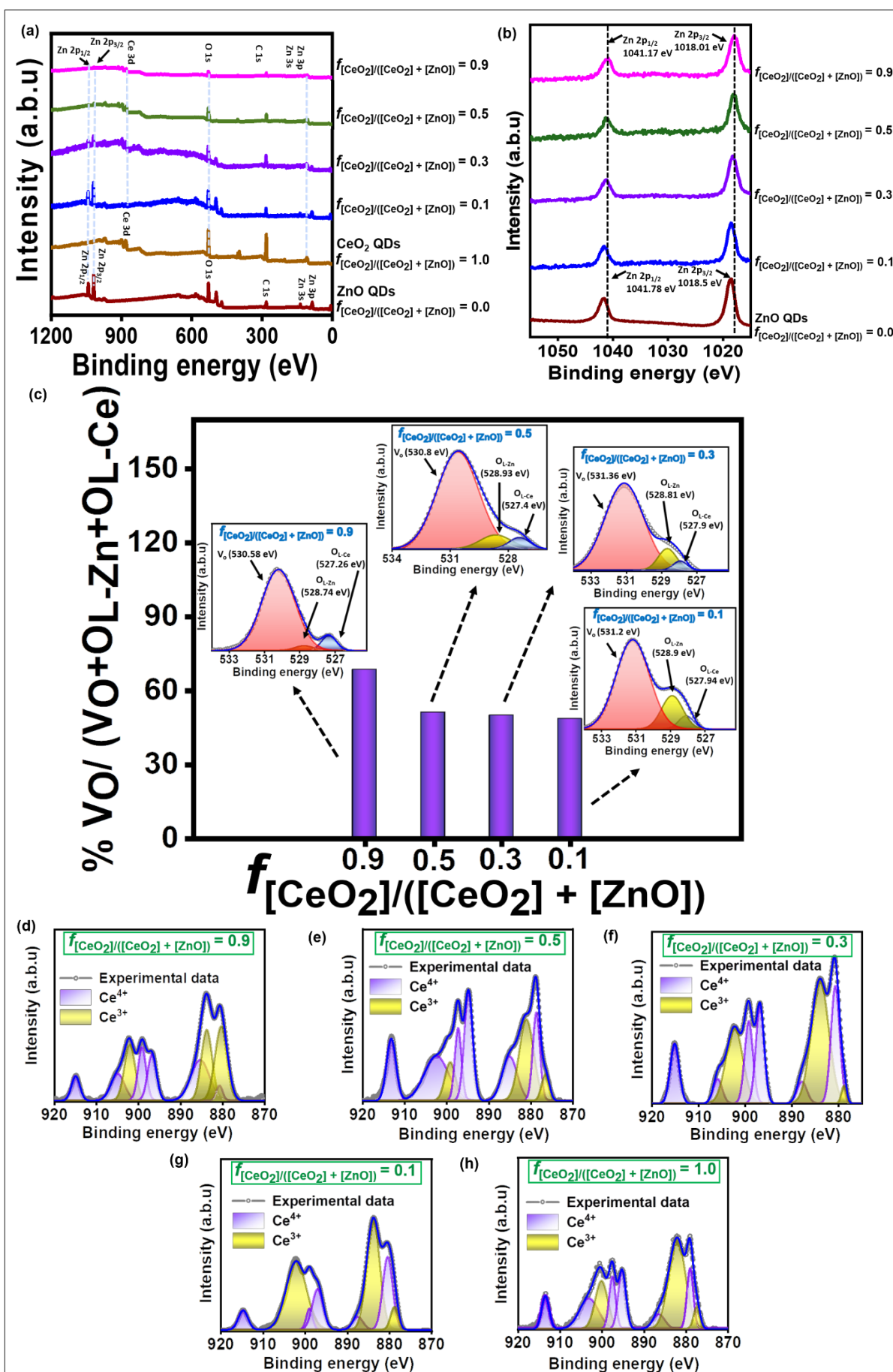
Figure 2. (a) XPS survey scan, **(b)** Zn 2p, and **(c)** Percentage of surface $V_O^\bullet$ estimated from the integrated area under the curve of O 1s for varying $[CeO_2]/[ZnO]$ ratios. O 1s spectral plots of $f_{[CeO_2]/([CeO_2]+[ZnO])}$ = 0.9, 0.5, 0.3, and 0.1 are given as insets. **(d-h)** Corresponding Ce 3d spectra of $f_{[CeO_2]/([CeO_2]+[ZnO])}$ = 0.9, 0.5, 0.3, 0.1, and 1.0.

Additionally, photoluminescence spectra of $V_O^\bullet$-$CeO_{2(x)}/ZnO_{(1-x)}@\beta$-CD QDs denote an intense yellow-green luminescence, marked by a prominent peak at 540 nm. The luminescence is particularly noticeable in samples containing 70% or more $V_O^\bullet$ rich-ZnO QDs, as confirmed by real-time images in Fig 3e. These spectral features closely mimic in vivo skin autofluorescence, necessarily endowing a foolproof camouflaging ability and evading the undesirable whitish tinge often left by commonly used sunscreens [28, 29]. In this way, the QD composites completely suppress the harmful UVA emission observed in conventional nano-ZnO, averting ROS-induced photo-aging and sunburn. The peak at 467 nm is interrelated with band edge transitions induced by abundant $V_O^\bullet$ in CeO_2 QDs, while that at 425 nm originates from the Ce 4f → O 2p transition (Fig 3d) [30]. As CeO_2 concentration rises, the PL intensity at 540 nm is weakened, accompanied by a concomitant rise in the intensity of the peak positioned at 467 nm. This indicates a diminishing number of radiative centres and underpins the importance of $V_O^\bullet$ as the key determinant in governing the photo-response of the QD composites. In view of the optimum UV-visible absorption, photoluminescence, and material performance, $V_O^\bullet$-$CeO_{2(0.3)}/ZnO_{(0.7)}@\beta$-CD QD composites or $f_{[CeO_2]/([CeO_2]+[ZnO])}$ = 0.3 fulfil all the technical requirements for their use as broadband UV blockers. Thus, $f_{[CeO_2]/([CeO_2]+[ZnO])}$ = 0.3 was employed for the remaining experiments hereafter, unless mentioned otherwise.
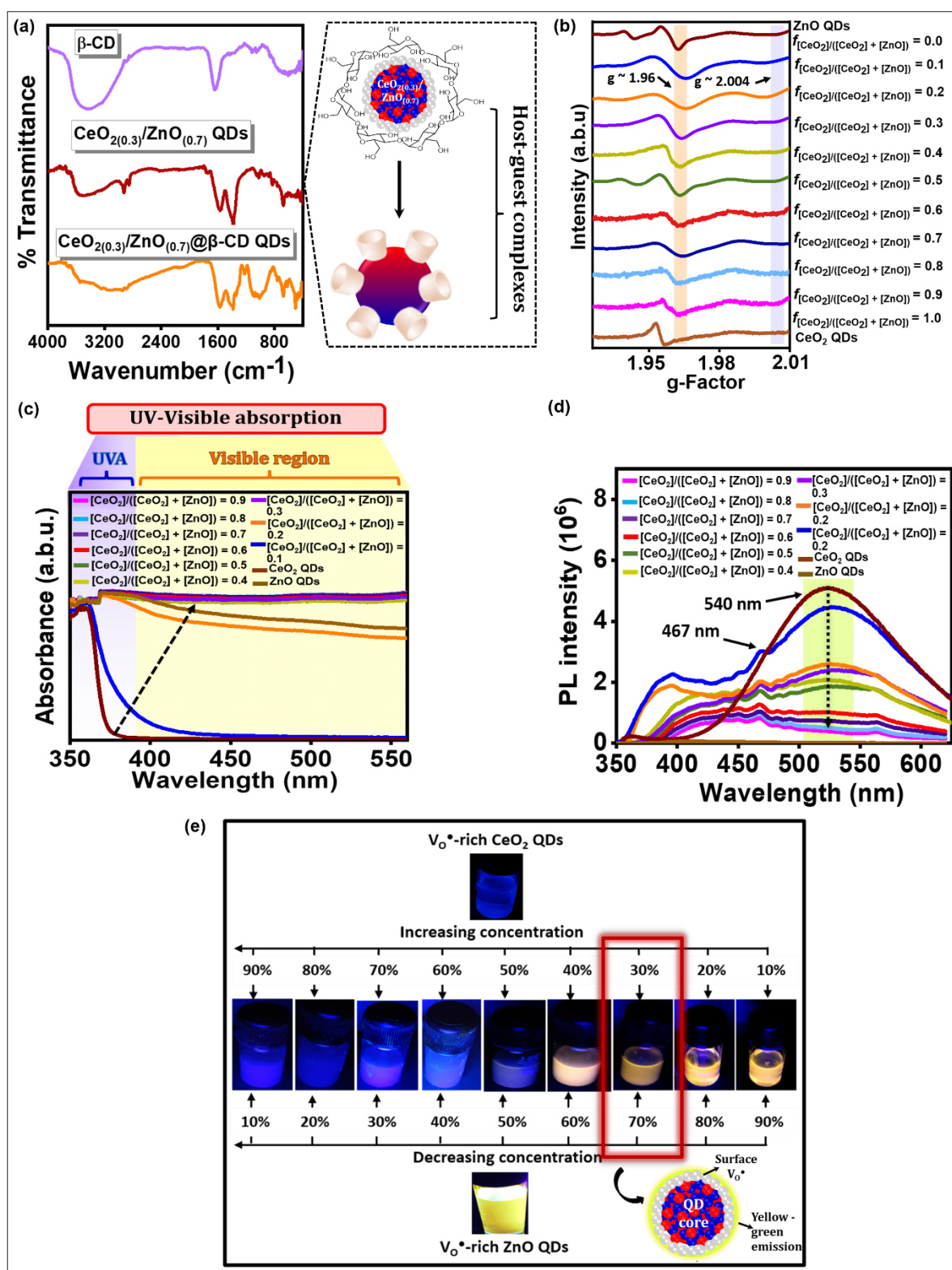
Figure 3. (a) FTIR, (b) EPR, (c) UV-visible absorption, and (d) photoluminescence spectra of $V_O{}^\bullet$-$CeO_{2(x)}$/$ZnO_{(1-x)}$@β-CD QD composites. (e) Digital photographs of the samples when subjected to UV irradiation with a handheld UV lamp (λ_{ex} = 365 nm) collating the varying photoluminescence for different % $V_O{}^\bullet$ rich-ZnO QDs.

3.4 Photostability studies

To better understand the photostability of UV irradiated-colloidal $V_O{}^\bullet$-$CeO_{2(0.3)}$/$ZnO_{(0.7)}$@β-CD QD composites under rigorous conditions, they are subjected to 10 hours of daily UV
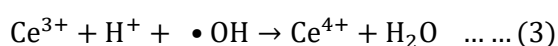
radiation (3 mW/cm^2) over 90 days, in conjunction with nano-TiO$_2$, nano-ZnO, and nano-CeO$_2$. The data in Table S1 depicts negligible variations in the normalized peak intensity and position throughout the experiment. V$_O$$^\bullet$-CeO$_{2(0.3)}$/ZnO$_{(0.7)}$@β-CD QD composites suspensions display resistance to photodegradation, with the normalized PL peak intensity decreasing by only 1.7% over 90 days, and emission maxima varied between 540 nm and 543 nm, respectively. In contrast, commercial nano-TiO$_2$, nano-ZnO, and nano-CeO$_2$ samples experience rapid photobleaching, with normalized PL intensity plummeting by 94%, 81%, and 64%, respectively, within a mere 10 h timeframe (Fig S4.). This photobleaching effect results from UVR-induced free radical generation, allude to inefficient UV protection by commercial nano-inorganic UV filters. Thus, V$_O$$^\bullet$-CeO$_{2(0.3)}$/ZnO$_{(0.7)}$@β-CD QD composites developed for the first time, is anticipated to alleviate UV-induced skin ailments. Therefore, delving into their biofunctionality in response to broad-spectrum UV radiation for an extended period is intriguing.

3.5 Analysis of surface modification and biostability

Surface functionalization of CeO$_{2(0.3)}$/ZnO$_{(0.7)}$ QD composites with β-CD was affirmed through FTIR spectra, comparing unmodified CeO$_{2(0.3)}$/ZnO$_{(0.7)}$ QDs, CeO$_{2(0.3)}$/ZnO$_{(0.7)}$@β-CD QD composites, and β-CD, represented in Fig 3a. The 3409 cm^{-1} broad peak in β-CD, attributed to O—H group, shifted slightly to 3440 cm^{-1} in CeO$_{2(0.3)}$/ZnO$_{(0.7)}$@β-CD QDs composites, demystifying successful conjugation. The vibrational mode at 2920 cm^{-1} (C—H stretching) and 1630 cm^{-1} (C=O) were observed in both β-CD and CeO$_{2(0.3)}$/ZnO$_{(0.7)}$@β-CD QDs composites. The bands at 1154 cm^{-1} and 1028 cm^{-1} belonged to C—O—C (glycosidic linkage) stretching, and C—O vibrations, respectively. The vibrational band at 935 cm^{-1} represented the characteristic R-1, 4-bond skeleton in β-CD. Deviations in Zn—O and Ce—O stretching modes to 670 cm^{-1} and 597 cm^{-1} in the fingerprint region implied adequate interaction of β-CD with CeO$_{2(0.3)}$/ZnO$_{(0.7)}$ QDs composites. Moreover, surface modification with truncated cone-structured β-CD underpins the long-lasting stability of nanoformulations in biofluids such as DMEM, SBF, and milli-Q. The zeta potential (ζ) of CeO$_{2(0.3)}$/ZnO$_{(0.7)}$@β-CD QD composites is -21.2 mV, attributed to the exclusive chemical structure of β-CD. Its hydrophobic cavity and a hydrophilic exterior surface facilitate the formation of β-CD-nanocrystal complexes (host-guest interaction), favouring electrostatic repulsive forces for optimal stabilization. Real-time digital photographs (Fig 4a.) taken on day 0 and after 120 days confirm the sustained stability of clear and homogeneous nanosuspensions in DMEM and SBF [31].

3.6 Cascade-like antioxidant effects of $V_O{}^\bullet$-CeO$_{2(0.3)}$/ZnO$_{(0.7)}$@β-CD QD composites — skin rejuvenation, anti-photoaging, and sunburn treatment

The appreciable structural, physiochemical, and UV protection attributes of $V_O{}^\bullet$-CeO$_{2(0.3)}$/ZnO$_{(0.7)}$@β-CD QD composites inspired us to investigate their bioactivity upon UV irradiation. First, the possibility of hydroxyl radical ($^\bullet$OH) scavenging under UVR exposure is assessed via terephthalic acid assay, according to the method described in section 2.4. The peak intensity associated with 2-hydroxy terephthalic acid (TAOH) is presumed to be proportional to the number of $^\bullet$OH generated. Fig 4b delineates the rapid quenching of the fluorescence of TAOH in presence of $V_O{}^\bullet$-CeO$_{2(0.3)}$/ZnO$_{(0.7)}$@β-CD QDs composites, evincing an encouraging ROS scavenging activity. Upon quantifying, it is confirmed that a significant 62.8% of $^\bullet$OH radicals are quenched within just 8 mins (Fig 4e). This can be ascribed to the reaction mechanism at the surface, involving the conversion of Ce^{3+} to Ce^{4+} through the consumption of $^\bullet$OH (quencher free radical) and H^+ from the surrounding media. Furthermore, the presence of surface $V_O{}^\bullet$ enables quick auto-regeneration of $Ce^{4+} \Leftrightarrow Ce^{3+}$, plausibly by lowering the reduction potential energy further, unveiling a promising cascading antioxidant effect. This unusual characteristic remains unparalleled in any UV filters hitherto identified for skin care applications. However, analogous antioxidative mechanisms were previously revealed for fuel cells rich with Ce^{3+} [32]. The plausible mechanism governing the $^\bullet$OH elimination performance of the QD composites, mitigating oxidative stress build-up in the intracellular milieu, is explained below:

$$Ce^{3+} + H^+ + \ ^\bullet OH \rightarrow Ce^{4+} + H_2O \quad ......(3)$$

Thus, this endows the QD composites with considerable potential as bioactive constituents for shielding the skin against UVRs, complemented by their salient antioxidant attributes.
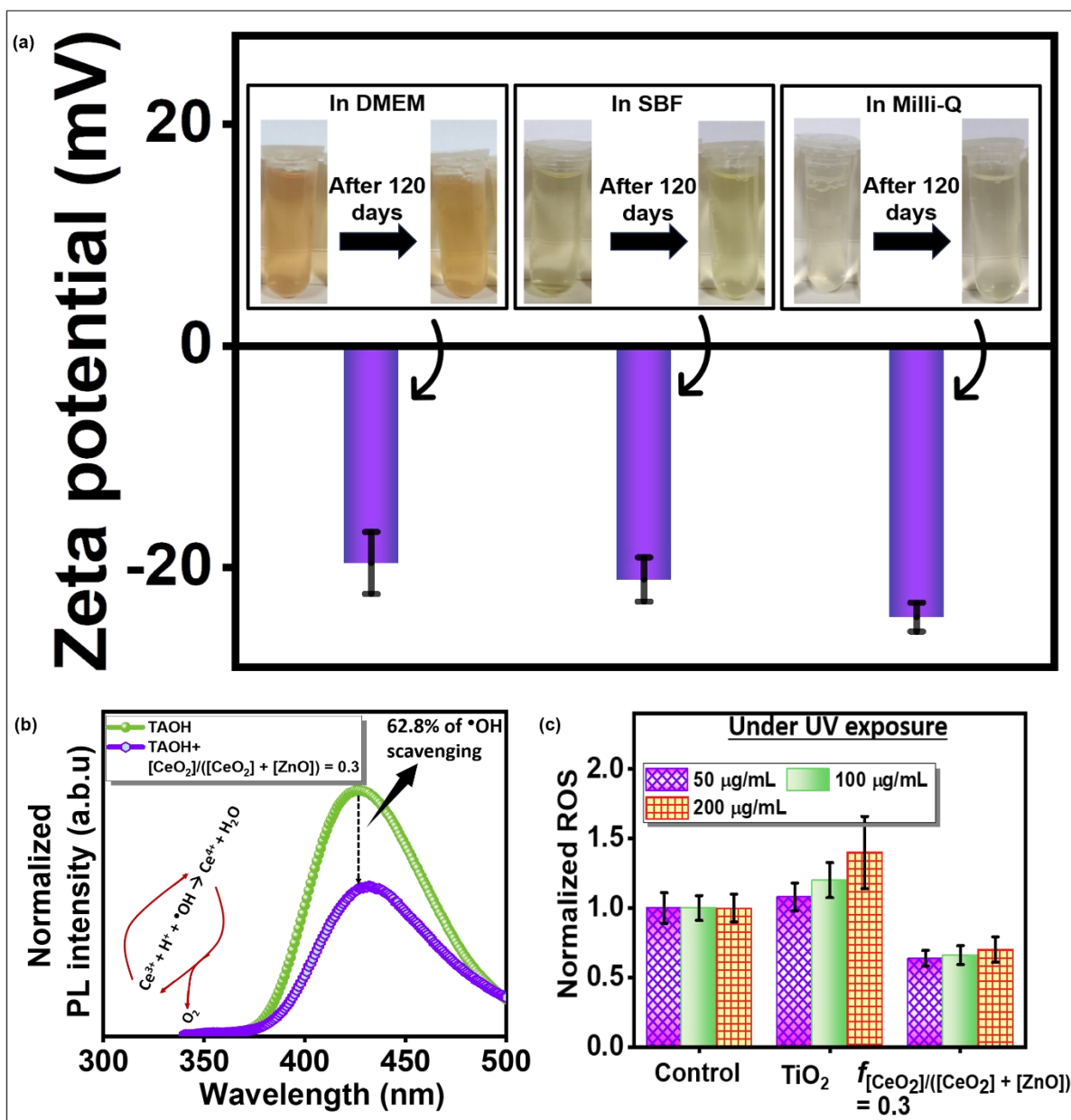
Figure 4. (a) Zeta potential of $V_O^\bullet$-$CeO_{2(0.3)}$/$ZnO_{(0.7)}$@β-CD QDs suspensions in DMEM, SBF, and Milli-Q (at day 0, room temperature and neutral pH). The inset shows digital photographs of the nanosuspensions at the first instance (day 0) and after 120 days to deduce the time-independent biostable nature. (b) PL spectral transitions of TAOH depicting the cascade-like hydroxyl radical scavenging activity commensurate with the reduction in the intensity in the presence of UVR. (c) Intracellular ROS scavenging potential of $V_O^\bullet$-$CeO_{2(0.3)}$/$ZnO_{(0.7)}$@β-CD QDs suspensions in HaCaT (human keratinocyte) cells relative to nano-TiO_2 — a conventional UV filter. It shows the protective effects of the QD composites against UV-induced ROS and their role in anti-photoaging. Error bars are represented as mean±SD.

To comprehend the possibility of intracellular oxidative stress in HaCaT cells induced by $V_O^\bullet$-$CeO_{2(0.3)}$/$ZnO_{(0.7)}$@β-CD QD composites under UV irradiation, a fluorescent probe-based-DCFDA assay is employed. Here, we acknowledge the well-explored photocatalytic activity of nano-TiO_2 under sunlight, which enhances intracellular ROS production. Thus, the experiments are performed in conjunction with TiO_2 as the benchmark in a simulated

environment to mimic the original conditions. Notably, a dose and $V_O^\bullet$ concentration-dependent increase in ROS levels in nano-TiO_2-treated HaCaT cells is observed, with the maximum at 200 μg/mL (Fig 4c). This explains the gravity of the toxicity concerns associated with recurrent and prolonged usage of nano-TiO_2-based sunscreens. Surprisingly, 200 μg/mL of $V_O^\bullet$-$CeO_{2(0.3)}$/$ZnO_{(0.7)}$@β-CD QD composites demonstrate a 30% ROS scavenging efficacy within 24 h. This aberrant photo-induced elimination of ROS is quite intricate and unique to $V_O^\bullet$-$CeO_{2(0.3)}$/$ZnO_{(0.7)}$@β-CD QDs composites, demonstrated for the first time in this work. It is believed to be the outcome of the $V_O^\bullet$-mediated band gap tailoring. The $V_O^\bullet$ act as electron traps that efficiently facilitates the separation of electrons and holes, reducing the photocatalytic ability. These free electrons at the surface then participate in the proton-coupled-electron-transfer (PCET) phenomena, accelerating the quenching of ROS [33-34]. PCET reactions at the reduced surfaces of TiO_2 and ZnO first observed by Schrauben et al., entails the simultaneous transfer of electrons and protons from the surrounding environment, thereby inducing subsequent redox reactions at the interface within the oxidizing system [35]. By extending this understanding to defect-rich surfaces of $CeO_{2(0.3)}$/$ZnO_{(0.7)}$@β-CD QDs composites, the ROS scavenging mechanisms can be delineated by these PCET reactions. In addition, Ce^{3+} at the surface engages in a replenishable redox reaction with endogenous H_2O_2, converting it to H_2O and O_2 while undergoing oxidation to Ce^{4+}, effectively combating hypoxia-mediated damage to skin cells. Based on the above results, it is exciting to note that the proposed material system unfolds a new possibility for naturally aiding skin rejuvenation and anti-photoaging through its enhanced in situ oxygen generation ability, expounded in Fig S3.

3.7 Efficacy and safety of $V_O^\bullet$-$CeO_{2(0.3)}$/$ZnO_{(0.7)}$@β-CD QD composites against UV-induced skin damage

The reduction in photoluminescence is observed in $V_O^\bullet$-$CeO_{2(x)}$/$ZnO_{(1-x)}$@β-CD QDs, as the $V_O^\bullet$-rich CeO_2 QDs concentration varies from 0 to 1, becoming almost imperceptible beyond 0.3. Meanwhile, anti-oxidant response experiences a modest increase until 0.4, followed by a significant upturn from 0.5 to 1. Consequently, an optimal $V_O^\bullet$-$CeO_{2(0.3)}$/$ZnO_{(0.7)}$@β-CD QDs composite is chosen to retain the best possible photoluminescence as well as biofunctionality. Section 3.7 elucidates the cumulative advantages of this chosen QD composite system based on our investigations in this study for a holistic assessment of its performance as a sunscreen active ingredient.

The cytoprotective efficacy of $V_O{}^\bullet$-$CeO_{2(0.3)}$/$ZnO_{(0.7)}$@β-CD QD composites is evaluated for skin protection. Phototoxicity experiments, simulating UVR-induced damage, are performed on HaCaT and L929 cells under UV radiations (3 mW/cm^2) and analyzed with MTT assay (Fig 5a-b). Nano-TiO$_2$ exhibit toxic effects on HaCaT and L929 cells, with a substantial decrease in live cell count from 36% (at 50 μg/mL) to 19% (at 200 μg/mL) and 31% (at 50 μg/mL) to 14% (at 200 μg/mL), respectively. Damage of keratinocytes is implicated in cutaneous malignancies, re-iterating the lethal impact of conventional UV filters, likely stemming from their deft photocatalytic response leading to ROS-induced cell apoptosis. A slightly diminished phototoxic effect of nano-TiO$_2$ is apparent in the absence of light exposure, contrasting with the commendable biocompatibility of $V_O{}^\bullet$-$CeO_{2(0.3)}$/$ZnO_{(0.7)}$@β-CD QDs composites. Comparative inspection of UV-exposed QD composites delineates impressively high cell survival rates, equal to or exceeding 90% for both cell lines.
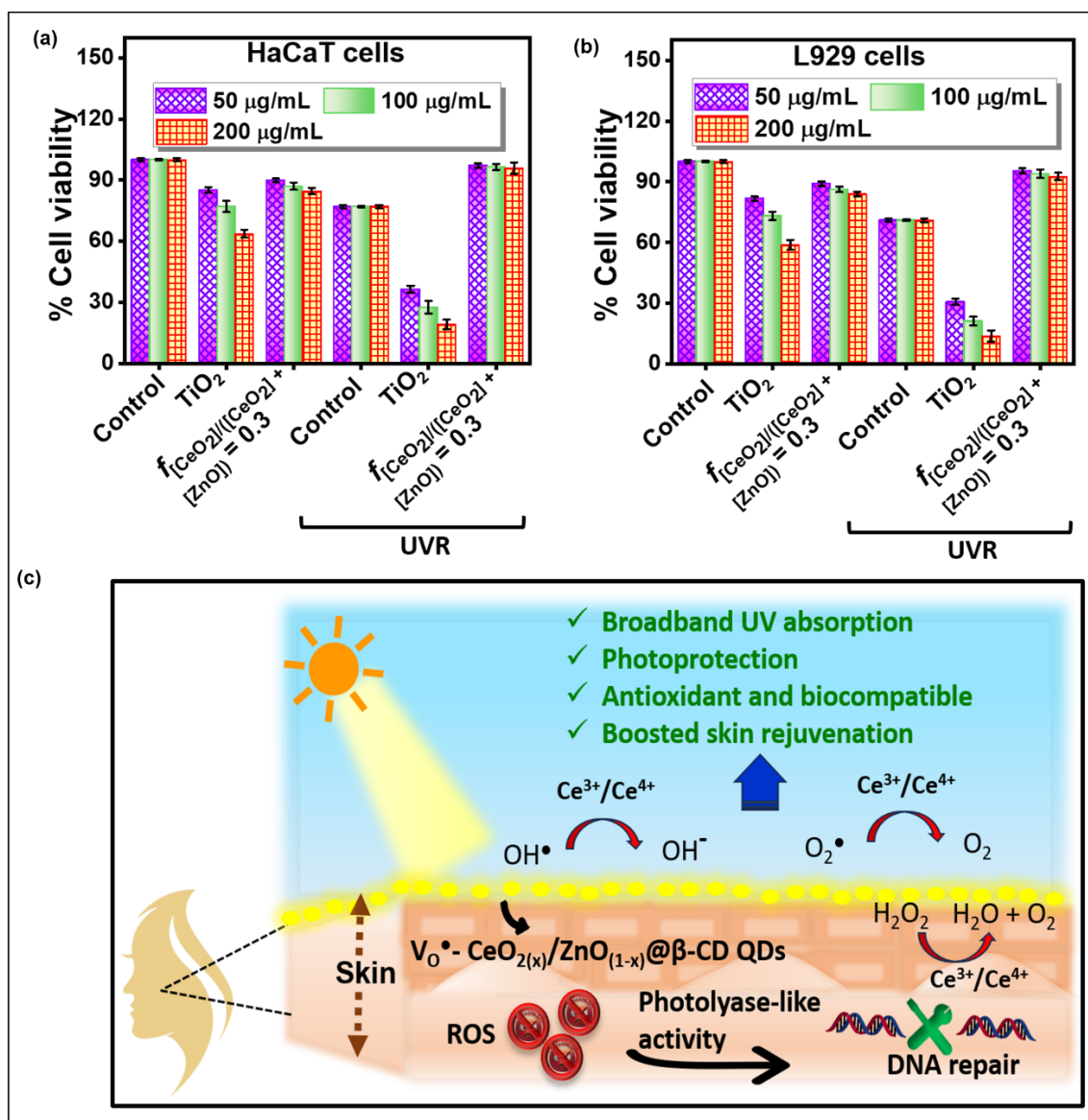
Figure 5. Cytotoxicity studies of $V_O{}^\bullet$-$CeO_{2(0.3)}$/$ZnO_{(0.7)}$@β-CD QD composites or $f_{[CeO_2]/([CeO_2]+[ZnO])} = 0.3$ relative to nano-TiO_2 in the dark and under UV exposure in (a) HaCaT and (b) L929 cells. (e) Schematic illustration describing $V_O{}^\bullet$-$CeO_{2(x)}$/$ZnO_{(1-x)}$@β-CD QD composites as the "miracle sunscreen" and the role of $V_O{}^\bullet$ or Ce^{3+}/Ce^{4+} for endowing them with proficient UV shielding, photostability, antioxidant, anti-aging potential and superior biosafety. Error bars are represented as mean±SD.

The susceptibility of human keratinocytes and mouse fibroblast cells to UV radiation is underscored by the *in vitro* MTT assay, indicating a substantial reduction in viability to 77% and 71%, respectively, following exposure to high UVR dose. Indeed, the percentage of viable cells treated with $V_O{}^\bullet$-$CeO_{2(0.3)}$/$ZnO_{(0.7)}$@β-CD QD composites under UVR is higher than in the absence of UVR and is cognizably reliant on the QD composites' surface $V_O{}^\bullet$ concentrations. This unusual phenomenon suggests the possibility of cell proliferation in the presence of UVR, challenging conventional understanding. The predominance of Ce^{3+} and $V_O{}^\bullet$ at the surface imparts photolyase-like mimicking potential to the QD composites. The inception of mid-gap states due to $V_O{}^\bullet$ inhibits electron-hole recombination, thereby supplementing the formation of photoelectrons [36]. These electrons play a crucial role in selectively cleaving the cyclobutane pyrimidine dimers. Simultaneously, the photolyase-like activity allows preferential repair of UV-damaged DNA, a feature previously unheard of in analogous systems but observed in porous nanorods of CeO_2 by Tian *et al* [37]. Furthermore, building upon the foundational notion of deleterious photo-induced ROS formation, Yew et al., elucidated the antioxidant capabilities of nanodiamonds, attributing it to their surface functional groups, whereas, lignin exhibited antioxidant characteristics owing to the phenolic groups [38]. Meanwhile, Son et al., modified the conventional inorganic physical UV blocker ─ TiO_2 with tannin to mitigate TiO_2's photocatalytic behaviour and render it with ROS scavenging potency [39]. Notwithstanding, Asok et al., devised a novel approach to boost the antioxidant property of ZnO QDs by deliberately introducing oxygen vacancy defects to tailor the surface chemistry [40]. Nevertheless, none of the contemporary active ingredients found in sunscreens have hitherto displayed engagement in antioxidative mechanisms that produce in situ O_2 within the biological milieu in a self-renewing fashion. On the other hand, it was observed that our proposed QD composites could rapidly scavenge H_2O_2 in presence of UV irradiation. This can be explained by the cascade-like antioxidant behaviour of $V_O{}^\bullet$-$CeO_{2(0.3)}$/$ZnO_{(0.7)}$@β-CD QDs composites, wherein, Ce^{3+} undergoes a quick auto-regenerative cycle, transitioning to Ce^{4+} and concurrently reducing H_2O_2 to H_2O and O_2 [41]. When this intracellular O_2 is generated in the skin keratinocyte cells, it counteracts UV-induced skin senescence, promotes revitalization of the skin through cell proliferation, and contributes to heightened skin sensorial properties. Clearly, these photochemical redox reactions reinforce the benign nature of the $V_O{}^\bullet$-

CeO$_{2(0.3)}$/ZnO$_{(0.7)}$@β-CD QD composites and their commendable photoprotective capabilities. Moreover, the host-guest complexes formed by β-CD proclaim controlled release behaviour, ameliorating biocompatibility [42-43].

3.8 V$_O$•-CeO$_{2(0.3)}$/ZnO$_{(0.7)}$@β-CD QD composites boosts performance of commercially available sunscreens

Taken together, V$_O$•-CeO$_{2(0.3)}$/ZnO$_{(0.7)}$@β-CD QD composites boast a myriad of functionalities that surpass those of existing nanostructure-based sunscreens. This superiority is attributed to the following factors: i) Apart from the broadband UV absorption and long-term photostability, they excel in camouflaging abilities, addressing the prevalent issue of white pigmentation associated with conventional micro and nano-inorganic UV filter-based sunscreens. ii) With respect to biofunctionalities, the QD composites advocate admirable antioxidant efficacy, UV-induced photoprotection, and biosafety akin to photolyase activity. Their distinctive cascade-like redox reactions yield H$_2$O and O$_2$. The endogenous O$_2$ produced, regardless of the UV exposure, naturally promotes cell growth, anti-photoaging, and rejuvenation of the skin, all in one. Thus, they act as "miracle sunscreen" endowed with multiple functionalities, unusually rare among UV filters reported to date. From an economic standpoint, utilizing this single-component, multipurpose sunscreen ingredient is significantly more cost-effective and reduces the toxicity concerns associated with the usage of multiple constituents.

The favourable corollaries from the aforementioned investigations of V$_O$•-CeO$_{2(0.3)}$/ZnO$_{(0.7)}$@β-CD QD composites have profoundly shaped a holistic outlook. To strengthen our proof-of-concept, we systematically compared the efficacy of V$_O$•-CeO$_{2(0.3)}$/ZnO$_{(0.7)}$@β-CD QD composite sunscreen with two commercial sunscreens based on nano-TiO$_2$ (CS1) and nano-Al$_2$O$_3$ (CS2). In Fig 6a, the characteristic emission maxima of CS1 appearing at 367 nm in the UVA region shift towards the visible spectrum upon mixing our customized ingredient. A manifold increment in the PL intensity is observed, completely circumventing UVA emission. Likewise, consistent PL spectral shifts of Al$_2$O$_3$-based-CS2 are discernible in presence of V$_O$•-CeO$_{2(0.3)}$/ZnO$_{(0.7)}$@β-CD QD composites (Fig 6a). This enunciates the higher potency of the QD composite-based formulations in broadband UV blocking compared to popularly used nano-inorganic UV filter sunscreens. Photographs from UV-induced rhodamine 6G (Rh6G) photocatalytic degradation studies depict the discolouration over 180 mins (Fig 6d). CS1 constituting nano-TiO$_2$ demonstrates the highest photobleaching, transitioning from fluorescent orange to a colourless Rh6G solution. This is in

sheer contrast to the marginal colour alteration noted for $V_O^\bullet$-CeO$_{2(0.3)}$/ZnO$_{(0.7)}$@β-CD QD composites. A high photocatalytic activity is associated with inferior UV shielding ability. Upon integration of the QD composite active ingredient with CS1 and CS2, a surprising inhibition in the photo-degradation was evinced. This signifies that $V_O^\bullet$-CeO$_{2(0.3)}$/ZnO$_{(0.7)}$@β-CD QD composite possesses unprecedented UV-blocking efficacy and improves the overall performance of commercial sunscreens (CS1 and CS2) as an additive. Conforming with the photocatalytic activity, intracellular UV-induced-ROS generation represents a 30% decline when the QD composite active ingredient is added.

Furthermore, there is a notable suppression in $^\bullet$OH generation, amounting to 80%, 84%, and 100% for CS1+$V_O^\bullet$-CeO$_{2(0.3)}$/ZnO$_{(0.7)}$@β-CD QDs composite, CS2+$V_O^\bullet$-CeO$_{2(0.3)}$/ZnO$_{(0.7)}$@β-CD QDs composite, and $V_O^\bullet$-CeO$_{2(0.3)}$/ZnO$_{(0.7)}$@β-CD QDs composite, respectively, in UVR (Fig 6b). This indicates the aberrant ROS scavenging efficacy of the QD composite active ingredient, minimizing the ROS-mediated carcinogenic effects of the commercial sunscreens. Cytotoxicity studies shown in Fig 6e-f, reveal a significant survival rate of 96%, 80%, and 84% for HaCaT cells treated with $V_O^\bullet$-CeO$_{2(0.3)}$/ZnO$_{(0.7)}$@β-CD QDs composite, CS1+$V_O^\bullet$-CeO$_{2(0.3)}$/ZnO$_{(0.7)}$@β-CD QDs composite, and CS2+$V_O^\bullet$-CeO$_{2(0.3)}$/ZnO$_{(0.7)}$@β-CD QDs composite, even after UV exposure. The consequences are nearly the same when these formulations are tested against L929 Cells. In contrast, CS1 and CS2 exhibit prominent phototoxicity, as conjectured by elevated cell mortality recognized in both cell types. In essence, $V_O^\bullet$-CeO$_{2(0.3)}$/ZnO$_{(0.7)}$@β-CD QDs composite, with diverse benefits encompassing broad-spectrum UV shielding, photostability, UV induced-ROS mitigation, biocompatibility, inhibition of photoaging, and skin replenishment, serves as a promising candidate for "smart" sunscreens and allied healthcare domains.
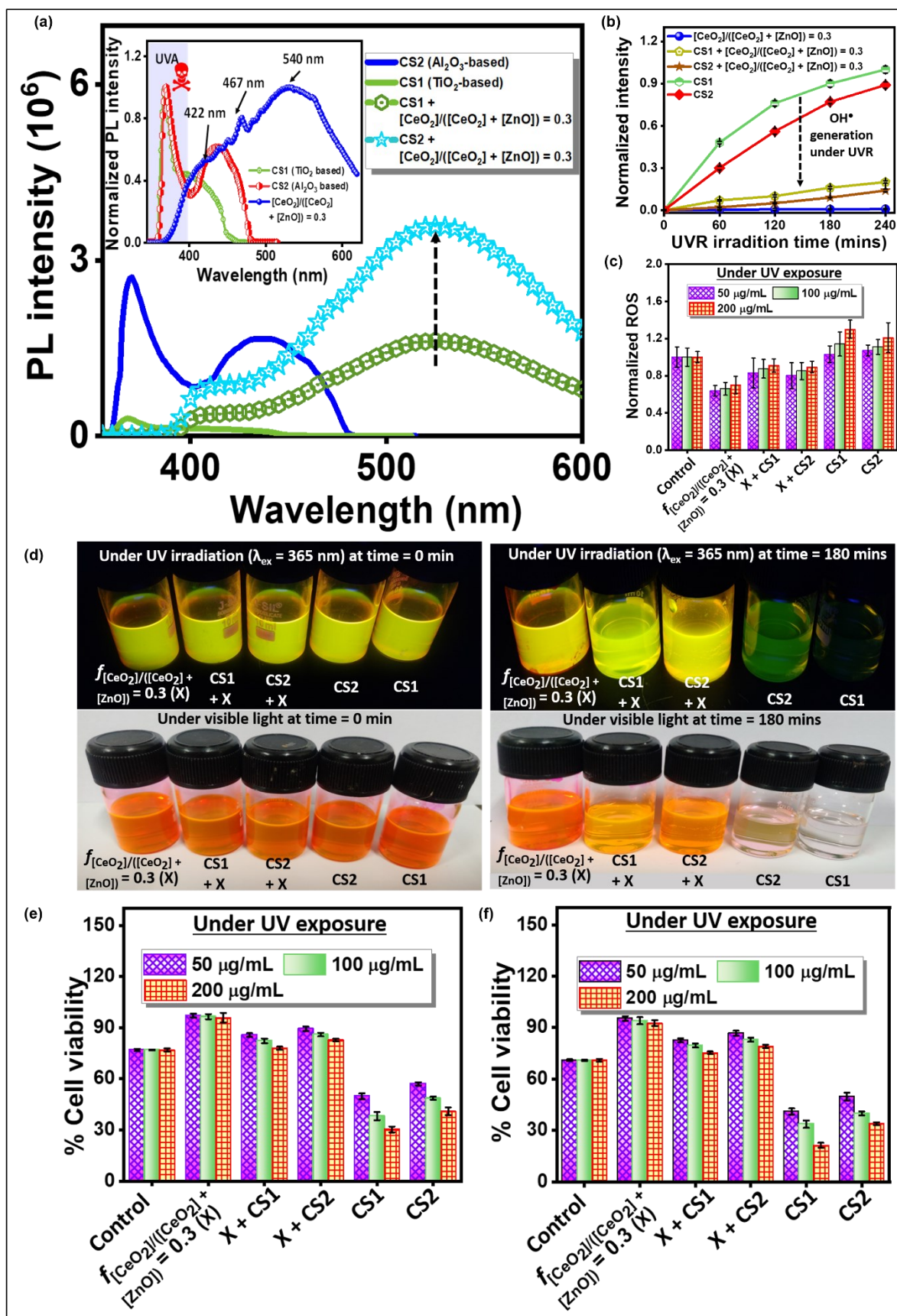
Figure 6. (a) Photo-response enhancement in the visible spectrum while suppressing the toxic UVA emission (related to ROS generation) of CS1 and CS2 by adding $V_O^\bullet$-$CeO_{2(0.3)}$/$ZnO_{(0.7)}$@β-CD QD composite. The normalized PL intensity plot is shown as an inset. (b) $^\bullet$OH generation tendency under UVR as a function of

exposure time (Dose of UVR: 3 mW/cm^2 for 4 h). (c) Intracellular ROS scavenging activity in the presence of UVR. (d) Digital photographs showing the photodegradation ability of rhodamine 6G under UVR exposure when treated with $V_O{}^\bullet$-CeO$_{2(0.3)}$/ZnO$_{(0.7)}$@β-CD QD composite (X), CS1, CS2, CS1+X, and CS2+X. No photobleaching is indicative of a higher photoprotection efficacy. Improvement in cytoprotection efficacy from UV damage is evaluated against (e) HaCaT and (f) L929 cells upon UVR exposure. Error bars are represented as mean±SD.

4. Conclusion

In this work, we harnessed the unique surface oxygen vacancy ($V_O{}^\bullet$)-rich defect chemistry of engineered CeO$_{2(x)}$/ZnO$_{(1-x)}$@β-CD QD composites to address the inherent challenges posed by prevailing sunscreens while incorporating additional benefits. The distinctive features of this material system have led us to consider it the "miracle sunscreen". A systematic materials characterization revealed the formation of phase-pure, monodispersed QDs, of which $V_O{}^\bullet$-CeO$_{2(0.3)}$/ZnO$_{(0.7)}$@β-CD QD composites demonstrated optimal physiochemical, optical, and bioactive performance. $V_O{}^\bullet$-CeO$_{2(0.3)}$/ZnO$_{(0.7)}$@β-CD QD composite contains a remarkable 49.8% surface $V_O{}^\bullet$, forming intermediate states to alter the bandgap energy, and facilitating electron-hole separation. UV-visible absorption and PL studies confirmed that this QD composite provides broad-spectrum UV shielding and long-term photostability. Additionally, it exhibits a strong visible emission at 540 nm, rendering a camouflaging ability to counteract the undesirable white tint associated with traditional nano-inorganic UV filters. At the same time, the inherent UV emission (370 nm) responsible for ROS-induced skin damage and photo-aging is bypassed entirely. Surprisingly, $V_O{}^\bullet$-CeO$_{2(0.3)}$/ZnO$_{(0.7)}$@β-CD QD composite scavenged a significant number of $^\bullet$OH radicals (62.8%) in presence of UVR, mitigating the risk of phototoxicity. More importantly, the intracellular cascade redox reaction by the Ce^{3+}/Ce^{4+} couple eliminated the noxious free radicals like H$_2$O$_2$ to H$_2$O and O$_2$. The generated O$_2$ effectively inhibited oxidative stress mediated-photoaging, promoted rapid skin rejuvenation and improved skin sensorial properties. The QD composites demonstrated incremented cell viability under UVR owing to photolyase-like mimetics, aiding in the repair of UV-damaged DNA and cell proliferation. The comparative analysis underpinned that the efficacy of $V_O{}^\bullet$-CeO$_{2(0.3)}$/ZnO$_{(0.7)}$@β-CD QD composite UV filter surpasses that of commercial sunscreens consisting of nano-TiO$_2$ and nano-Al$_2$O$_3$, offering several benefits. These advantages encompass broadband photoprotection for prolonged duration by suppressing the characteristic UVA emission known to be carcinogenic, antioxidant properties, non-phototoxicity, and skin-friendly features. Thus, this study offers a new paradigm for designing economical, benign, and efficacious multifunctional UV filters for next-generation sunscreen formulations.

Declaration of Competing Interest

The authors have no potential conflicts of interest to declare.

Data availability

Data will be made available on request.

References:

[1] Dong, Y., Chen, S., Zhou, S., Hou, S. and Lu, Q., Perspectives on the next generation of sunscreen: Safe, broadband, and long-term photostability. ACS Materials Letters, 1(3) (2019), 336-343.

[2] Gao, Q. and Garcia-Pichel, F., Microbial ultraviolet sunscreens. Nature Reviews Microbiology, 9(11) (2011), 791-802.

[3] Bernhard, G.H., Neale, R.E., Barnes, P.W., Neale, P.J., Zepp, R.G., Wilson, S.R., Andrady, A.L., Bais, A.F., McKenzie, R.L., Aucamp, P.J. and Young, P.J., Environmental effects of stratospheric ozone depletion, UV radiation and interactions with climate change: UNEP Environmental Effects Assessment Panel, update 2019. Photochemical & Photobiological Sciences, 19(5) (2020), 542-584.

[4] Lyons, A.B., Trullas, C., Kohli, I., Hamzavi, I.H. and Lim, H.W., Photoprotection beyond ultraviolet radiation: a review of tinted sunscreens. Journal of the American academy of dermatology, 84(5) (2021), 1393-1397.

[5] World Health Organization, Ultraviolet radiation and the INTERSUN Programme, http://www.who.int/uv/faq/skincancer/en/index1.html (accessed: Jan 2024).

[6] Santos, A.C., Marto, J., Cha-Cha, R., Martins, A.M., Pereira-Silva, M., Ribeiro, H.M. and Veiga, F., Nanotechnology-based sunscreens—A review. Materials Today Chemistry, 23 (2022), 100709.

[7] Yamada, M., Mohammed, Y. and Prow, T.W., Advances and controversies in studying sunscreen delivery and toxicity. Advanced Drug Delivery Reviews, 153 (2020), 72-86.

[8] Gao, W., Wang, Z., Tan, G., Liu, W., Sendeku, M.G., Tang, Y., Kuang, Y. and Sun, X., Dual Functional Titanium Hydride Particles for Anti-Ultraviolet and Anti-Oxidant Applications. Advanced Functional Materials, 2023, 2209422.

[9] Sarkar, S., Debnath, S.K., Srivastava, R. and Kulkarni, A.R., Continuous flow scale-up of biofunctionalized defective ZnO quantum dots: A safer inorganic ingredient for skin UV protection. Acta Biomaterialia, 147 (2022), 377-390.

[10] Feng, Y., Zhang, D., Chen, X., Zhou, C. and Liu, M., Confined-Synthesis of Ceria in Tubular Nanoclays for UV Protection and Anti-Biofilm Application. Advanced Functional Materials, 2023, 2307157.

[11] Truffault, L., Ta, M.T., Devers, T., Konstantinov, K., Harel, V., Simmonard, C., Andreazza, C., Nevirkovets, I.P., Pineau, A., Veron, O. and Blondeau, J.P., Application of nanostructured Ca doped CeO2 for ultraviolet filtration. Materials Research Bulletin, 45(5) (2010), 527-535.

[12] Cardillo, D., Sencadas, V., Devers, T., Islam, M.M., Tehei, M., Rosenfeld, A., Boutard, T., Rocher, E., Barker, P.J. and Konstantinov, K., Attenuation of UV absorption by poly (lactic acid)-iron oxide nanocomposite particles and their potential application in sunscreens. Chemical Engineering Journal, 405 (2021), 126843.

[13] Ji, Q.T., Mu, X.F., Hu, D.K., Fan, L.J., Xiang, S.Z., Ye, H.J., Gao, X.H. and Wang, P.Y., Fabrication of host–guest complexes between adamantane-functionalized 1, 3, 4-oxadiazoles and β-cyclodextrin with improved control efficiency against intractable plant bacterial diseases. ACS Applied Materials & Interfaces, 14(2) (2022), 2564-2577.

[14] Ma, W., Mashimo, T., Tamura, S., Tokuda, M., Yoda, S., Tsushida, M., Koinuma, M., Kubota, A., Isobe, H. and Yoshiasa, A., Cerium oxide (CeO_{2-x}) nanoparticles with high Ce^{3+} proportion synthesized by pulsed plasma in liquid. Ceramics International, 46(17) (2020), 26502-26510.

[15] Anirban, S. and Dutta, A., Structural and ionic transport mechanism of rare earth doped cerium oxide nanomaterials: Effect of ionic radius of dopant cations. Solid State Ionics, 309 (2017), 137-145.

[16] Kabir, F., Murtaza, A., Saeed, A., Ghani, A., Ali, A., Khan, S., Li, K., Zhao, Q., Yao, K.K., Zhang, Y. and Yang, S., Structural, optical and magnetic behavior of (Pr, Fe) co-doped ZnO based dilute magnetic semiconducting nanocrystals. Ceramics International, 48(14) (2022), 19606-19617.

[17] Thanh, N.T., Maclean, N. and Mahiddine, S., Mechanisms of nucleation and growth of nanoparticles in solution. Chemical reviews, 114(15) (2014), 7610-7630.

[18] Guo, X., Chen, X., Liu, P., Zhou, H., Fu, S., Li, W., Liu, X., Ma, F. and Wu, Z., Preparation and mechanical properties of copper matrix composites reinforced by carbon nanotubes and Al2O3. Advanced Engineering Materials, 23(6) (2021), 2001490.

[19] Bahador, A., Umeda, J., Hamzah, E., Yusof, F., Li, X. and Kondoh, K., Synergistic strengthening mechanisms of copper matrix composites with TiO2 nanoparticles. Materials Science and Engineering: A, 772 (2020), 138797.

[20] Bonnet, E., Grenier, J.C., Bassat, J.M., Jacob, A., Delatouche, B. and Bourdais, S., On the ionic conductivity of some zirconia-derived high-entropy oxides. Journal of the European Ceramic Society, 41(8) (2021), 4505-4515.

[21] Yang, C., Woottapanit, P., Cao, J., Yue, Y., Zhang, D., Yi, J., Zeng, Z., Zhang, X., Qin, J. and Wang, Y., In situ formation of a ZnS/In interphase for reversible Zn metal anodes at ultrahigh currents and capacities. Journal of Materials Chemistry A, 11(45) (2023), 24902-24910.

[22] Hao, Y.J., Ma, Y.G., Zhang, X., Li, J., Wang, S., Chen, X. and Li, F.T., Unraveling the importance between electronic intensity and oxygen vacancy on photothermocatalytic toluene oxidation over CeO_2. Chemical Engineering Journal, 433 (2022), 134619.

[23] Sun, Y.F., Li, J.J., Xie, F., Wei, Y. and Yang, M., Ruthenium-loaded cerium dioxide nanocomposites with rich oxygen vacancies promoted the highly sensitive electrochemical detection of Hg (II). Sensors and Actuators B: Chemical, 320 (2020), 128355.

[24] Ranjbari, A., Demeestere, K., Kim, K.H. and Heynderickx, P.M., Oxygen vacancy modification of commercial ZnO by hydrogen reduction for the removal of thiabendazole: Characterization and kinetic study. Applied Catalysis B: Environmental, 324 (2023), 122265.

[25] Chen, X., Liu, L., Yu, P.Y. and Mao, S.S., Increasing solar absorption for photocatalysis with black hydrogenated titanium dioxide nanocrystals. Science, 331(6018) (2011), 746-750.

[26] Meng, N., Huang, Y., Liu, Y., Yu, Y. and Zhang, B., Electrosynthesis of urea from nitrite and CO_2 over oxygen vacancy-rich ZnO porous nanosheets. Cell Reports Physical Science, 2(3) (2021), 100378.

[27] Li, M., Wang, P., Ji, Z., Zhou, Z., Xia, Y., Li, Y. and Zhan, S., Efficient photocatalytic oxygen activation by oxygen-vacancy-rich CeO_2-based heterojunctions: Synergistic effect of photoexcited electrons transfer and oxygen chemisorption. Applied Catalysis B: Environmental, 289 (2021), 120020.

[28] Zeng, H., MacAulay, C., Palcic, B. and McLean, D.I., Spectroscopic and microscopic characteristics of human skin autofluorescence emission. Photochemistry and photobiology, 61(6) (1995), 639-645.

[29] Leffell, D.J., Stetz, M.L., Milstone, L.M. and Deckelbaum, L.I., In vivo fluorescence of human skin: a potential marker of photoaging. Archives of dermatology, 124(10) (1988), 1514-1518.

[30] El Desouky, F.G., Saadeldin, M.M., Mahdy, M.A., Abd El Wahab, S.M. and El Zawawi, I.K., Impact of calcination temperature on the structure, optical and photoluminescence properties of Nanocrystalline Cerium oxide thin films. Materials Science in Semiconductor Processing, 111 (2020), 104991.

[31] Jiang, L., Rahnama, M., Zhang, B., Zhu, X., Sui, P.C., Ye, D.D. and Djilali, N., Predicting the interaction between nanoparticles in shear flow using lattice Boltzmann method and Derjaguin–Landau–Verwey–Overbeek (DLVO) theory. Physics of Fluids, 32(4) (2020), 043302.

[32] Xu, K., Pei, S., Zhang, W., Han, Z., Guan, P., Wang, L., Zou, Y., Ding, H., Ma, X., Xu, C. and Liu, F., Ce (III)-terephthalic acid metal-organic frameworks as highly efficient· OH radical scavengers for fuel cells and investigation of its antioxidation mechanism. Materials today energy, 31 (2023), 101195.

[33] Agarwal, R.G., Kim, H.J. and Mayer, J.M., Nanoparticle O–H Bond Dissociation Free Energies from Equilibrium Measurements of Cerium Oxide Colloids. Journal of the American Chemical Society, 143(7) (2021), 2896-2907.

[34] Warburton, R.E., Mayer, J.M. and Hammes-Schiffer, S., Proton-coupled defects impact O–H bond dissociation free energies on metal oxide surfaces. The Journal of Physical Chemistry Letters, 12(40) (2021), 9761-9767.

[35] Schrauben, J.N., Hayoun, R., Valdez, C.N., Braten, M., Fridley, L. and Mayer, J.M., Titanium and zinc oxide nanoparticles are proton-coupled electron transfer agents. Science, 336(6086) (2012), 1298-1301.

[36] Huo, H., He, Y., Chen, W., Wu, L., Yi, X. and Wang, J., Simultaneously monitoring UVC-induced DNA damage and photoenzymatic repair of cyclobutane pyrimidine dimers by electrochemical impedance spectroscopy. Talanta, 239 (2022), 123081.

[37] Tian, Z., Yao, T., Qu, C., Zhang, S., Li, X. and Qu, Y., Photolyase-like catalytic behavior of CeO_2. Nano Letters, 19(11) (2019), 8270-8277.

[38] Yew, P.Y.M., Zhu, D.D., Lin, Q.Y., Jiang, L., Chee, P.L., Leong, H.S., Dong, Z., Guo, X.D., Kai, D. and Loh, X.J., Synergistic UV protection effects of the lignin nanodiamond complex. Materials Today Chemistry, 22 (2021), 100574.

[39] Son, H.Y., Koo, B.I., Lee, J.B., Kim, K.R., Kim, W., Jang, J., Yoon, M.S., Cho, J.W. and Nam, Y.S., Tannin–titanium oxide multilayer as a photochemically suppressed ultraviolet filter. ACS applied materials & interfaces, 10(32 (2018), 27344-27354.

[40] Asok, A., Ghosh, S., More, P.A., Chopade, B.A., Gandhi, M.N. and Kulkarni, A.R., Surface defect rich ZnO quantum dots as antioxidants inhibiting α-amylase and α-glucosidase: a potential anti-diabetic nanomedicine. Journal of materials chemistry B, 3(22) (2015), 4597-4606.

[41] Liu, J., Ye, L.Y., Xiong, W.H., Liu, T., Yang, H. and Lei, J., A cerium oxide@ metal–organic framework nanoenzyme as a tandem catalyst for enhanced photodynamic therapy. Chemical Communications, 57(22) (2021), 2820-2823.

[42] Yi, S., Zheng, J., Lv, P., Zhang, D., Zheng, X., Zhang, Y. and Liao, R., Controlled drug release from cyclodextrin-gated mesoporous silica nanoparticles based on switchable host–guest interactions. Bioconjugate chemistry, 29(9) (2018), 2884-2891.

[43] Radu, C.D., Parteni, O. and Ochiuz, L., Applications of cyclodextrins in medical textiles. Journal of Controlled Release, 224 (2016), 146-157.